IOP Publishing Physics in Medicine and Biology

Phys. Med. Biol. **52** (2007) 3579–3600 doi:10.1088/0031-9155/52/12/016

Model-based respiratory motion compensation for emission tomography image reconstruction

M Reyes[1,4], G Malandain[1], P M Koulibaly[2], M A González-Ballester[3] and J Darcourt[2]

[1] Asclepios Team, INRIA, Sophia Antipolis, France
[2] Nuclear Medicine Department at Centre Antoine Lacassagne, Nice, France
[3] MEM Research Center, Institute for Surgical Technology and Biomechanics, University of Bern, Switzerland

E-mail: Mauricio.Reyes@memcenter.unibe.ch

Received 24 October 2006, in final form 21 March 2007
Published 23 May 2007
Online at stacks.iop.org/PMB/52/3579

Abstract

In emission tomography imaging, respiratory motion causes artifacts in lungs and cardiac reconstructed images, which lead to misinterpretations, imprecise diagnosis, impairing of fusion with other modalities, etc. Solutions like respiratory gating, correlated dynamic PET techniques, list-mode data based techniques and others have been tested, which lead to improvements over the spatial activity distribution in lungs lesions, but which have the disadvantages of requiring additional instrumentation or the need of discarding part of the projection data used for reconstruction. The objective of this study is to incorporate respiratory motion compensation directly into the image reconstruction process, without any additional acquisition protocol consideration. To this end, we propose an extension to the maximum likelihood expectation maximization (MLEM) algorithm that includes a respiratory motion model, which takes into account the displacements and volume deformations produced by the respiratory motion during the data acquisition process. We present results from synthetic simulations incorporating real respiratory motion as well as from phantom and patient data.

M This article features online multimedia enhancements

(Some figures in this article are in colour only in the electronic version)

[4] Currently at MEM Research Center, Institute for Surgical Technology and Biomechanics, University of Bern, Switzerland.

1. Introduction

The motivation of this work is the early diagnosis of tumors in lungs. Early diagnosis is essential since it increases the probability of therapy success. However, respiratory motion during the data acquisition process leads to blurred images, making diagnosis, planning and following more difficult. The scenario is worst if small tumors are to be detected. For instance, Osman *et al* (2003) investigated the impact of motion during the examination, finding mislocalizations of lesions in the fusion of positron emission tomography (PET) and transmission computerized tomography (CT). Similarly, significant tumor motion has been reported in other studies, e.g. Shih *et al* (2002), Shimizu *et al* (2000), Balter *et al* (1996), Seppenwoolde *et al* (2002). Nehmeh and colleagues also reported a significant volume increase of lung lesions in images reconstructed without respiratory motion compensation (Nehmeh *et al* 2002).

Current methods can be classified into the following categories: post-processing, filtered back projection (FBP)-based methods, multiple acquisition frame (MAF), sinogram data selection, sinogram correction and incorporated-motion-model (IMM)-based methods.

Post-processing methods are based on transformations applied on the reconstructed images. These transformations are typical found aiming at improving the image fusion between different modalities. A typical example of this is the image fusion of PET-CT images, where the PET image presents a blurring component due to respiratory motion during the data acquisition process, whereas the CT image does not or in a much lesser degree and can be thought of as a motion-free image. The image registration procedure then deals with motion compensation indirectly trying to warp the PET image into the CT one. Due to the elastic nature of lungs and the deformation of the thoracic cavity under respiratory motion, nonlinear registration techniques have shown to perform better than rigid or affine transformations (Mattes *et al* 2003, Camara *et al* 2002). On the other hand, nonlinear registration method techniques can compensate for shape differences due to the motion, but do not fully compensate for all the motion's effects, since the reconstruction itself has been intrinsically and definitively impaired by the motion.

FBP-based methods work on the projection space (Crawford *et al* 1996, Lu and Mackie 2002). These methods are based on a modified filtered backprojection algorithm that considers respiratory motion as a time-varying magnification and displacement in the anterior–posterior and lateral directions, which is too simplistic considering the elastic and non-homogeneity of motion within the thorax. The main drawback of these methods is that the motion model is not really coupled to the reconstruction algorithm, and thus the reconstruction algorithm must be modified to adapt it, hindering further adaptations of the method to more complex or specific motion models.

More realistic are the MAF-based methods (Picard and Thompson 1997, Pellot-Barakat *et al* 2001). They consist in regrouping the projections into smaller subsets according to the detected motion. Then, the image reconstruction of each subset is performed independently and is followed by realignment of the images to fuse all reconstructions. The MAF-based approaches present the inconvenience that the signal-to-noise ratio decreases for images reconstructed from smaller subsets of projections, leading to intermediate images suffering from heavy noise. Besides, these methods require the data to be acquired specially in a set of frames for the purpose of motion compensation, which does not allow us to perform motion compensation in a retrospective way in data acquired in a normal clinical set-up.

Sinogram data selection based on motion detection, also known as gating, has been used to compensate for motion correction in ET (Nehmeh *et al* 2002, 2003, Visvikis *et al* 2003). Respiratory gating (Nehmeh *et al* 2002) synchronizes the breathing cycle with

the data acquisition process by using a respiratory motion tracking device. In respiratory-correlated dynamic PET (Nehmeh *et al* 2003), the tracking of an external FDG source point situated over the patient's thorax allows us to correlate with the patient's breathing motion. Gating techniques have shown improvements in reducing the blurring effect caused by motion, contributing to a better quantification of lesions. However, they require extra hardware or specific data acquisition modes and they discard some data for the image reconstruction. Besides, it has been shown that using tracking devices based on external information (e.g. elasticized belt, skin markers, etc) may not always correlate with lung tumor location (Berbeco *et al* 2005, Vedam *et al* 2003), which has motivated the use of more complex tracking device systems (e.g. implanted radio-opaque markers). In Visvikis *et al* (2003), an approach based on *a posteriori* respiratory motion gating of dynamic PET images was presented, which does not need an external signal to perform the gating of data. In this method, a Fourier analysis of the acquired PET dynamic data allows us to estimate the respiratory frequency, from which projection data can be retrospectively selected (*a posteriori* gating). However, the method requires user interaction in order to carefully select a region-of-interest (ROI) on which the time activity curve is analyzed.

Other approaches are based on sinogram correction. These methodologies act directly on the projection data by repositioning the lines-of-response (LOR) when the motion is known (Qi and Huesman 2002, Rahmim and Bloomfield 2003, Thielemans *et al* 2003, Lamare *et al* 2007). However, these approaches are only applicable to rigid or affine motions and require to deal with motion-corrected LORs that may fall in non-valid positions. Although this issue was solved in Qi and Huesman (2002), there is still the constraint of rigid motions, which decreases their practical interest for respiratory motion compensation.

IMM-based methods, as can be seen in Jacobson and Fessler (2003), Qiao *et al* (2006), Li *et al* (2006), Gilland *et al* (2002), Cao *et al* (2003), Gravier and Yang (2005), Gravier *et al* (2006), employ a motion model coupled to the image reconstruction process. This makes these types of techniques very appealing since they perform at once a single optimization for the acquired data and the motion compensation. In Gilland *et al* (2002), Cao *et al* (2003), the motion model is incorporated through spatial and bio-mechanical-based penalty terms, whereas in Gravier and Yang (2005), Gravier *et al* (2006) motion information is incorporated through a temporal prior functional in a maximum-*a-posteriori* (MAP) framework. These techniques have been tested for gated cardiac applications yielding reconstructed images with improved quality. However, it has been remarked that the parameter associated with the prior/penalty term needs careful selection and plays an important role in the final reconstructed image (Qiao *et al* 2006). In addition, these techniques still need to be tested for respiratory motion compensation.

On the other hand, the approaches presented in Jacobson and Fessler (2003), Qiao *et al* (2006), Li *et al* (2006) consider the motion model as a part of the system model of photon detection probabilities. In Jacobson and Fessler (2003), joint maximum likelihood of image and deformation parameters is performed. Motion is modeled through an image transformation matrix that is dependent on a set of unknown parameters. The image transformation matrix is proposed to be constructed as compositions of interpolation functions and affine expressions of the unknown parameters. In Qiao *et al* (2006) and Li *et al* (2006), a more practical implementation is proposed. The motion model is constructed by performing non-rigid registration on 4D-CT data of the patient. This way, motion information from different phases of the breathing cycle can be retrieved and then used in the image reconstruction step. The main drawback of these approaches is the need of the 4D-CT scan to construct each time the motion model.

The purpose of this paper is to describe a reconstruction algorithm that allows for a retrospective respiratory motion compensation, which does not require any specific acquisition protocol or discarding of data for the reconstruction. In regard to how motion information is incorporated within the image reconstruction process, the method follows the ideas initially presented by Rahmim *et al* (2004), and then extended in Li *et al* (2006) and Qiao *et al* (2006). The main novelties of the proposed method are mainly twofold. First, a respiratory motion model is constructed from two MRI image frames. Motion information of a particular patient is then retrieved by adapting this model to the patient anatomy through affine registration. This, in turn, allows retrospective motion compensation on data acquired without any other type of complementary motion information (e.g., 4D CT scans, respiratory tracking devices) nor temporal tags associated with the acquired data (e.g., list-mode). Second, the method is able to take into account not only displacements but also local deformations through a voxel model designed to adapt itself accordingly to the deformations produced by respiratory motion.

The next sections present the methodology and results from synthetic simulations incorporating real respiratory motion, phantom and patient data, as well as conclusions and perspectives.

2. Method

2.1. Maximum likelihood expectation maximization

First introduced in emission tomography by Shepp and Vardi (1982), the MLEM algorithm is based on a *Poisson* model for the emission process. For a given emission element b (that we also identify as a voxel), the number of emissions f_b follows a Poisson law with mean λ_b. Besides, each scalar term R_{db} of the projection matrix $\mathbf{R}$ (or called by some authors *system matrix* or *transition matrix*) gives the probability that a certain emission from voxel b is detected by the detector unit, or detector tube, d.[5]

The number of detections from the detector tube d (i.e., p_d) can be expressed in terms of the number of emissions f_b as follows:

$$p_d = \sum_b f_b R_{db}. \tag{1}$$

Equation (1) is important since it states the relationship between detections and emissions through the system matrix values.

We are interested in finding the mean value $\hat{\boldsymbol{\lambda}}$ from the set of projections $\mathbf{p}$. This can be done by searching the maximum likelihood of getting a set of measures $\mathbf{p}$ given an image $\boldsymbol{\lambda}$,

$$\hat{\boldsymbol{\lambda}} = \arg\max_{\boldsymbol{\lambda}} [P(\mathbf{p}|\boldsymbol{\lambda})]. \tag{2}$$

It can be shown (see Shepp and Vardi (1982) for more details) that the maximization of (2) can be conducted by means of an iterative algorithm

$$\lambda_b^{\langle K+1\rangle} = \frac{\lambda_b^{\langle K\rangle}}{\sum_d R_{db}} \sum_d \frac{p_d R_{db}}{\sum_{b'} \lambda_{b'}^{\langle K\rangle} R_{db'}}, \tag{3}$$

where p_d stands for the number of detections from detector tube d, λ_b is the estimated mean number of emissions from voxel b, R_{db} is the probability that a particle emitted from voxel b is detected by d and K stands for the iteration number. Further correction factors and

[5] For annihilation coincidence detection the detector tube is defined by the two photons detected in coincidence, whereas for single photon detection, collimation is used to define it (Shepp and Vardi 1982).

regularization schemes can be added to (3). We perform attenuation correction according to Levkovitz *et al* (2001) in which weights are computed based on an attenuation map (typically a CT scan). This methodology is revisited in the next section to account for motion. Regularization is performed by means of image convolution with a Gaussian kernel (Reader *et al* 2002, Levkovitz *et al* 2001).

2.2. Incorporating motion compensation into MLEM

We incorporate motion compensation into the MLEM algorithm (Shepp and Vardi 1982) through the projection matrix $\mathbf{R}$. As was stated, each element R_{db} of this matrix represents the probability that a particle emitted from voxel b is detected by detector tube d. To account for motion, each of these terms is computed by considering the motion that each voxel performs during data acquisition. The new contribution term, R^m_{db}, reflects the interactions voxel/detector-tube under motion.

To describe the motion each voxel suffers, let us first consider a continuous motion modeled by the spatio-temporal transformation $\varphi : \mathbb{R}_+ \times \mathbb{R}^3 \mapsto \mathbb{R}^3$, where $\varphi(t, \mathbf{m}) = \varphi_t(\mathbf{m})$ denotes the position of a point $\mathbf{m} = (x, y, z)$ at time t. The motion is observed from time $t = 0$ to $t = T$. This motion is then discretized in a set of N spatial transformations $\varphi : \mathbb{N} \times \mathbb{R}^3 \mapsto \mathbb{R}^3$, where $\varphi(i, b) = \varphi_i(b)$ describes the position of voxel b at time i $(i = 0, \ldots, N-1)$, and φ_i being valid from $t = t_i$ to $t = t_{i+1}$. N denotes the number of motion states that discretize the continuous motion.

The discrete transformations φ_i allow us to construct R^m_{db} as the weighted sum of partial contributions R^i_{db} of deformed voxels $\varphi_i(b)$ as follows:

$$R^m_{db} = \sum_i w_i R^i_{db}. \tag{4}$$

The weights $w_i = (t_{i+1} - t_i)/T$ allow to take into account the kinetic of the motion: $w_i T$ represents the duration where φ_t can be effectively approximated by φ_i.

2.3. Computation of system matrix terms

The voxels that contribute to detector tube d are assumed to intersect a line in 3D. Let us denote by l_{db} the intersection length of this line with the emission element b. We thus define the contribution of b to d by

$$\text{static:} \quad R_{db} = \frac{l_{db}}{\sum_{d'} l_{d'b}} \qquad \text{dynamic:} \quad R^i_{db} = \frac{l^i_{db}}{\sum_{d'} l^i_{d'b}}. \tag{5}$$

In the static case, we model the emissions elements as spheres inscribed in voxels (see figure 1(a)), which facilitates the calculation of (5) (see appendix A). The summation in each denominator of (5) allows to compute the probability values from length measures l_{db}.

To take into account the motion, one has to compute the contribution of the moving emission element b to each detector tube d (5). If no deformations occur, computation of R^i_{db} can be performed by considering the intersection between a line and a sphere-shaped voxel. However, this is not realistic since it has been shown that the displacements in the thorax (due to the respiratory motion) present a nonlinear and a non-homogeneous behavior (Seppenwoolde *et al* 2002, Weruaga *et al* 2003). Thus, the voxel deformation has to be considered. Unfortunately, the shapes of deformed cubic or spherical voxels are too complex to enable an easy computation of the intersection. However, the spherical model allows us to approximate the deformed voxel as ellipsoids (see figure 1(b)), whose deformation can be easily obtained by studying the gradient of $\varphi_i, \nabla\varphi_i$ (see appendix B

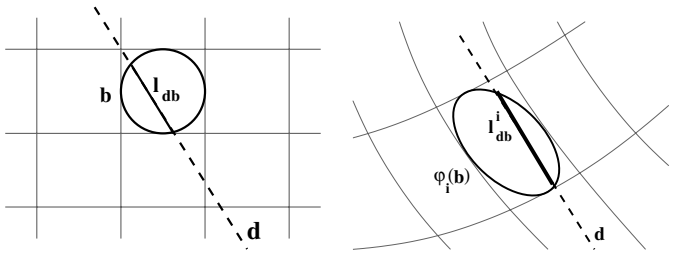

Figure 1. The contribution of an emission element b to a detector tube d, represented by a dotted line, is defined by the intersection (continuous line) of (a) a sphere with a line (static case) or, (b) an ellipsoid (a deformed sphere) with a line (dynamic case).

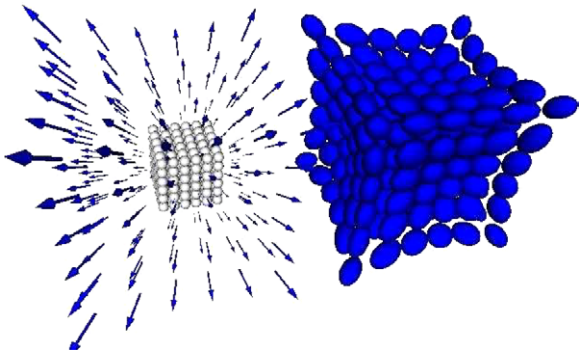

Figure 2. Testing the deformation of a set of sphere-shape-modeled emission elements following a pre-built DVF. Left: original and displacement vector field. Right: emission elements after transformation.

for more details). Indeed, let us consider the singular value decomposition (SVD) of the matrix $\nabla\varphi_i$, that is $\nabla\varphi_i = U\Sigma V^T$, where U and V are square and orthogonal matrices and $\Sigma = \mathrm{diag}(\delta_1, \delta_2, \delta_3)$, with δ_j, $j = \{1, 2, 3\}$ the singular values of $\nabla\varphi_i$. It turns out that the columns of U are the eigenvectors of $\nabla\varphi_i \nabla\varphi_i^T$, which also give the preferred local deformation directions, while the δ_j are related to the magnitude of the deformations in the direction of the eigenvectors.

In practice, one normally disposes of a displacement vector field (DVF) $\psi_i : \mathbb{N} \times \mathbb{R}^3 \mapsto \mathbb{R}^3$, that describes the marginal displacement of a voxel in space during time interval i. The matrix $\nabla\varphi_i$ can be easily obtained by $\nabla\varphi_i = Id + \nabla\psi_i$, with Id the identity matrix.

Figure 2 shows a test in which emission elements have been modeled as spheres and deformed into ellipsoids with a pre-built displacement vector field.

The modeling of the emission elements as spheres that translate and deform locally into ellipsoids according to a given DVF, represents a novel contribution. Furthermore, since a closed form exists to compute the intersection between a line and an ellipsoid (see appendix A), computations of the system matrix elements are faster than those using classical methods of intersection (e.g. Siddon algorithm (Siddon 1985)) used by others, e.g. (Reader *et al* 2002, Herman and Odhner 1991). This is of great importance since the motion compensation methodology requires to compute the projection matrix terms for each time state, so storage of several projection matrices is prohibitive. The situation is even worse when one deals with

fully 3D image reconstruction, which would require computation and storage of a very large projection matrix.

Under the model assumptions, we consider that the number of decays per voxel maintains during deformation, but its distribution changes. Indeed, a spheroid changing its volume so that it fills completely or partially two or more regular voxels (static case), will distribute the number of decays between these voxels. This precisely permits the retrospective correction through the interaction between voxels and detector elements as indicated by (5). The model does not account for elasticity properties of tissues (e.g., Young's modulus and Poisson's ratio), which we consider does not contribute greatly due to the current detection system resolution capacities.

2.4. Estimation of the respiratory motion

In practice, unless extra devices are used to measure the breathing pattern, the respiratory motion (transformation φ) is generally unknown. A first approach to estimate this motion consisted in registering a known respiratory motion model on the data to be reconstructed. To build this model, two MRI images of a volunteer were acquired at breath holding in expiration and inspiration and then non-rigidly registered with an iconic feature-based non-rigid algorithm (Cachier *et al* 2003). This provides us with a volumetric DVF ψ. Transformations $\Phi_i(b)$, describing the position of a voxel b at time state i, are then obtained by linear interpolation

$$\Phi_i(b) = b + \frac{i}{N}\psi(b). \tag{6}$$

To adapt the transformation Φ_i to a patient, we found two alternatives. The first one considers the creation of an average image of the model expiration and inspiration states (to simulate a non-corrected reconstruction) that is affinely registered against the non-corrected functional reconstructed patient's image. The second alternative uses an existing attenuation map acquired with breath holding, generally at inspiration, which is then registered with the inspiration image of the model. For both cases the registration is performed on the segmented lungs. No inter-modality registration issues are then expected to appear when performing the affine registration.

The affine registration was performed with a block-matching-based algorithm. It uses a least square estimator and the correlation coefficient as similarity measure (Ourselin *et al* 2000). This provides us with an affine transformation T. We compose then the transformations to obtain

$$\varphi_i = T \circ \Phi_i \circ T^{-1}. \tag{7}$$

To illustrate these steps, figure 3 shows the adaptation performed between the simplified model and the patient's attenuation map.

Though this method is by no means robust since it is sensitive to the selection of the anatomy and physiology of the person from where the motion model is created, it provides a preliminary insight of the results that can be achieved by using such an approximative model in conjunction with the motion compensation technique used here. In regard to this matter, further improvements and work in progress are discussed later.

2.5. Attenuation correction

In general terms, the value μ_b in an attenuation map $\mu(x)$ represents the linear attenuation coefficient of voxel b. As is also known, this coefficient represents the fraction of a beam of gamma rays that is absorbed or scattered when it passes through voxel b. This coefficient

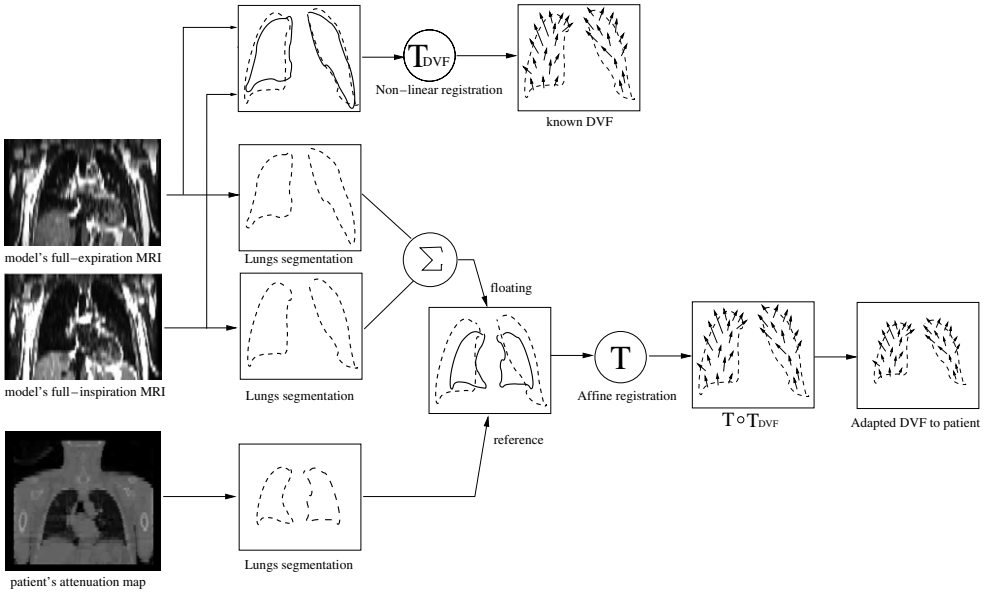

Figure 3. Adapting a known respiratory displacement vector field to patient anatomy. Two MRI images corresponding to full-expiration and full-inspiration are non-rigidly registered (T_{DVF} transformation), the resulting displacement vector field (labeled as 'known DVF') is then adapted to the patient anatomy by means of an affine transformation (i.e. $T \circ T_{DVF}$). In practice, the patient's anatomical image can be the patient's attenuation map used later for attenuation correction of the ET reconstructed image.

is dependent on the tissue type the particular voxel represents. For annihilation coincident detection systems, the attenuation experienced by a pair of photons along a detector tube d can be written as

$$\exp\left(-\int_d \mu(x)\,\mathrm{d}x\right), \tag{8}$$

which can be approximated to

$$\exp\left(\sum_b -l_{db}\mu_b\right). \tag{9}$$

In the presence of motion, we must take into account the displacements and deformations of emission elements. To do so, we compute attenuation correction weights a_d^i associated with the detector tube d to each time state i

$$a_d^i = \exp\left(\sum_b l_{db}^i \mu_b\right), \tag{10}$$

with μ_b assumed to be measured at the reference state.

This way, the attenuation correction can be incorporated into the reconstruction step by modifying (4), as follows,

$$R_{db}^{m,\mathrm{att}} = \sum_i w_i a_d^i R_{db}^i. \tag{11}$$

Finally, by replacing the term R_{db} in (3) by $R_{db}^{m,\mathrm{att}}$ or R_{db}^m, we incorporate motion compensation with or without attenuation correction, respectively.

(a) (b) (c)

Figure 4. Sagittal (a), axial (b) and coronal (c) activity image planes of the reference volume image with a lesion modeled as a sphere with a diameter of 15 mm.

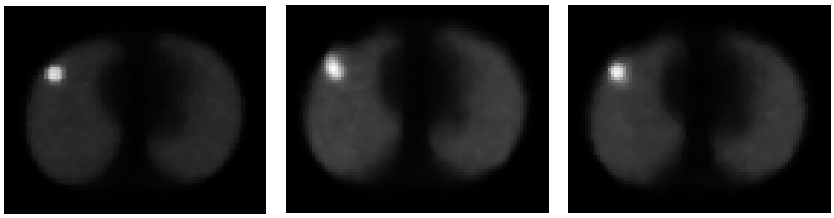

(a) (b) (c)

Figure 5. Image reconstruction of reference frame (static) (a), without motion compensation (b) and with motion compensation (c).

3. Results

3.1. Motion correction for simulated and real data

3.1.1. Simulated data. We simulated respiratory motion in a SPECT study of lungs. For this, we used the thorax phantom *NCAT* (Segars 2001) (*NURBS-based cardiac torso*). It is a model of the human thorax anatomy and physiology, which was created for the nuclear medicine imaging research. To the NCAT phantom a small lesion of 15 mm diameter with a background-to-lesion-activity of 1:8 was added. Figure 4 shows the activity image for the reference state.

The model was then deformed with N transformations φ_i, $i = 0, \ldots, N-1$ (equation (7)), which were estimated from the known real respiratory motion transformation Φ (equation (6)). Sinograms were computed for each time state using the SimSET (*Simulation System for Emission Tomography*) library (Harrison *et al* 1993) and then combined into one single sinogram by a weighted sum.

The images were reconstructed with the MLEM algorithm without and with motion correction. Regularization was performed by means of iterative Gaussian filtering every two iterations with a full-width at half-maximum (FWHM) of 8.0 mm. These parameters were found by visual inspection of the image profiles around the hot spot of images reconstructed with different sets of regularization parameters.

No other correction was included for the image reconstruction. The reconstructed 3D images have a size of $128 \times 128 \times 128$ voxels with a voxel size of $3 \times 3 \times 3$ mm^3.

Figure 5 shows, from left to right, the reconstructed reference image (motion-free), the reconstructed image without motion compensation, and with motion compensation. As described in the literature, the lesion appears larger in the non-corrected reconstruction (Nehmeh *et al* 2002). Indeed, the measured relative volume error with respect to the reference image was of 23.8%. After motion compensation it decreased to 1%, with a centroid error

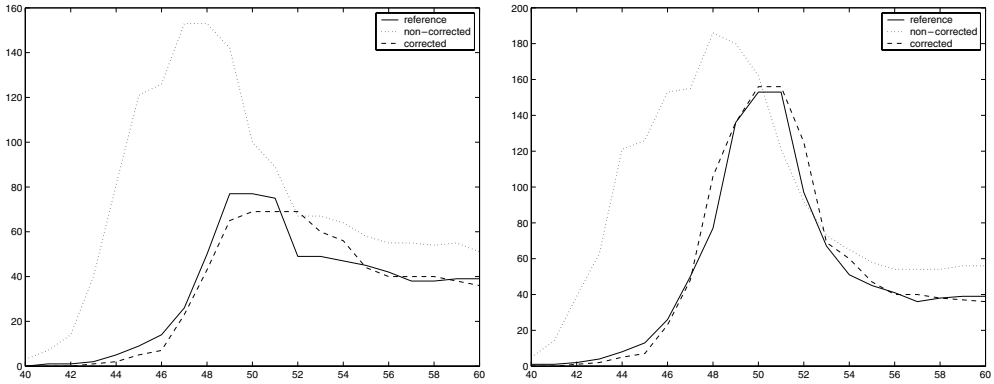

(a) x-coordinate: 34 (b) x-coordinate: 35

Figure 6. Intensity profiles for axial slice 43 around the lesion area. After 20 MLEM iterations the corrected profiles (dashed line) show a close relationship with the reference profiles (continuous line) in comparison with the non-corrected profile (dotted line).

before motion compensation of 2.49 voxels (7.5 mm) and of 0.45 voxels (1.5 mm) after motion compensation.

Motion compensation was also applied without considering voxels deforming as ellipsoids, but only displacements. In terms of volume error with respect to the reference image, an increase from 1% (considering voxels deforming into ellipsoids) to 5.36% (considering non-deforming voxels) was found. This result agrees with the inspection of values of the Jacobian, which has a physical interpretation in terms of the local volume variation (Rey *et al* 2002), computed on transformation φ over the lesion area. As an average, an expansion factor of 1.06 was found, meaning that the local volume expansion in the lesion region is on average 6%.

A visual comparison of the intensity profiles (figure 6) shows a good fit between the motion-corrected and the ground truth intensity spatial distributions.

To better assess the results, a qualitative study based on a fuzzy c-means segmentation of the lesion was performed. It is a segmentation technique based on fuzzy logic. The user provides the number of sets upon which the data are segmented (e.g. three sets for background, lung tissues and lesion tissues), the intensity centroid for each set, level of overlap between sets and an error threshold to stop the iterations (Ahmed *et al* 2002). Isosurfaces were generated for the reference volume (i.e., expiration state) and for the non-corrected and corrected reconstructed volumes (figure 7). From figure 7 it can be seen the improvements in terms of shape correction obtained after motion compensation. As can also be seen in figure 6, a good fit between the reference image (i.e., motion-free reconstructed image) and the motion-compensated image is noticeable.

Two figures of merit were used to measure quantitatively the performance of the motion compensation methodology, namely the coefficient of variability (CV), defined by $\mathrm{CV} = \sigma(\text{lesion})/\mu(\text{lesion})$ where $\mu(\text{lesion})$ and $\sigma(\text{lesion})$ denote the average and the standard deviation of the intensity values over the lesion, and the contrast recovery (CR), defined by $\mathrm{CR} = \mu(\text{lesion})/\mu(\text{background})$ (Levkovitz *et al* 2001). Table 1 shows the CR and CV values obtained for the reference, non-corrected and corrected reconstructed images with respect to the number of intermediate states (N) used for the image reconstruction.

From the CV values shown in table 1, we found that for the simulated data noise properties of the reconstructed images were not affected by the motion compensation technique. Higher

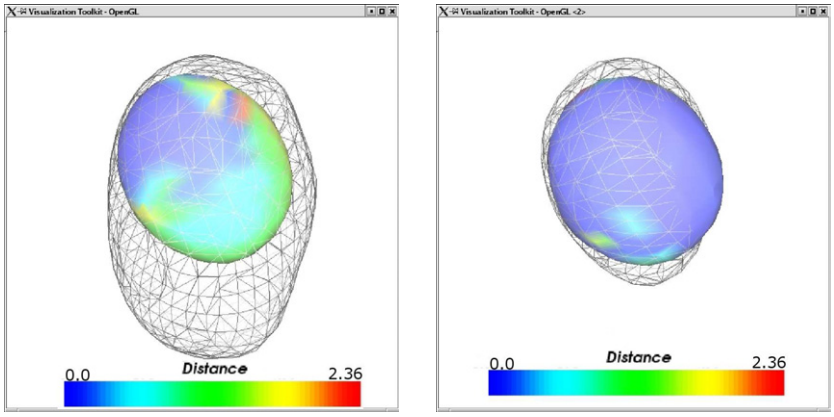

(a) Non-corrected (b) Corrected

Figure 7. Comparison of the reconstructed lesion volumes (a) without motion compensation and (b) with motion compensation for the activity volume shown in figure 4. Iso-surfaces extracted from reconstructed images are rendered in wire frame, while the one extracted from the reference is colored. The color indicates the distance between the two displayed surfaces, i.e. an error between the reference lesion and the reconstructed one.

Table 1. Coefficient of variability (CV) and contrast recovery (CR) values for the reference, non-corrected and corrected reconstructions for different numbers of motion states (N).

			Corrected				
	Reference	Non-corrected	$N = 2$	$N = 3$	$N = 4$	$N = 5$	$N = 6$
CR	5.80	3.20	4.10	4.35	4.40	4.30	4.40
CV	0.14	0.13	0.14	0.14	0.13	0.14	0.13

CR values are found for the corrected cases in comparison with the non-corrected one ($27 \pm 4\%$ of increment), which demonstrates the deblurring effect of the motion compensation technique. It can also be noticed that from a certain point onwards, an increment in the number of times used to discretize the motion does not considerably improve the reconstruction.

3.1.2. Influence of the registration step on the motion-compensated lesion activity distribution. The matching between the respiratory motion model with the patient anatomy involves a step of affine registration (see figure 3). Our concern was to measure the influence of the errors introduced due to this step in the reconstructed images. The hypothesis is that an increase in volume due to an error in the registration step should produce a decrease in the mean intensity of the lesion activity, and vice versa. To check this hypothesis, errors were introduced in the form of an affine transformation, which was applied to the adapted DVF (7). Then, image segmentation performed by thresholding at a fixed percentage of maximum intensity was performed in order to measure volume and mean intensity of the lesion volume. The affine matrix has the following parameters:

$$\begin{pmatrix} 1+e & 0 & 0 & a \\ 0 & 1+f & 0 & 0 \\ 0 & b & 1+g & 0 \\ 0 & 0 & 0 & 1 \end{pmatrix}. \tag{12}$$

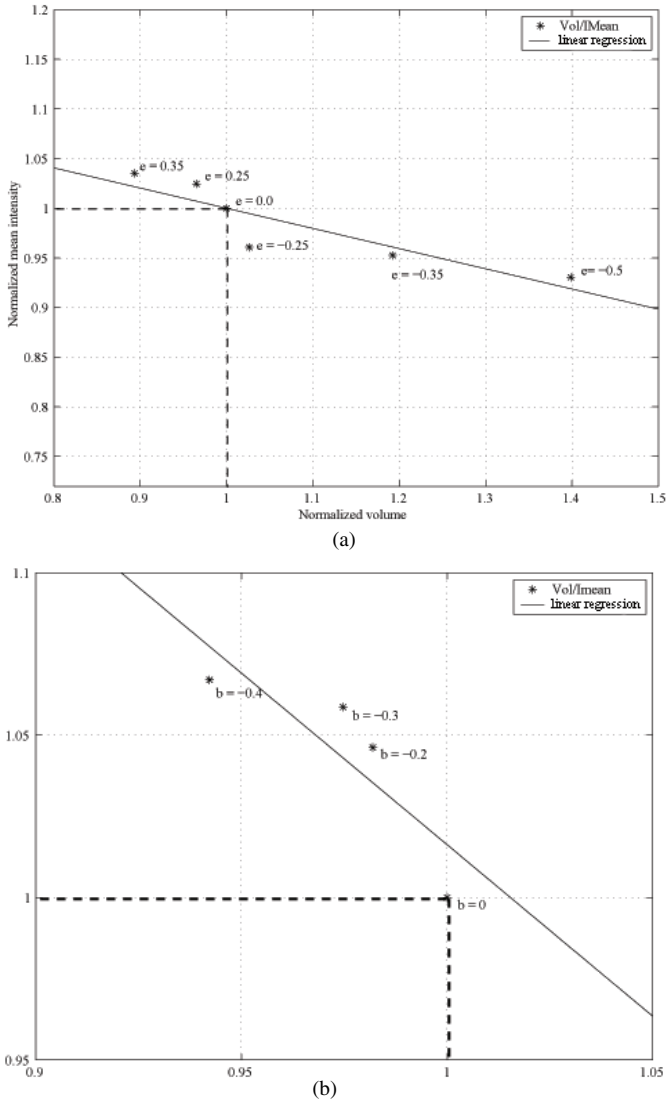

Figure 8. Testing the influence of matching errors in the step of affine image registration (see figure 3). A known affine transformation (equation (12)) was set with three different configurations of parameters (varying one parameter (a), (b), and a mixture of them (c)) and applied to the patient-adapted DVF. The plots show that an increase in volume produces a decrease in intensity.

For simulated data, three tests were carried out: varying only the parameter e, varying only the parameter b, and a combination of different variations in the parameters (see figure 8). From figure 8 the expected inverse relation between lesion volume and mean intensity increase can be seen. However, due to the effects of noise in the reconstructed images, the points do not fall exactly in a line, but the tendency is clearly visualized.

3.1.3. Phantom data. A phantom made of three spheres filled with 99mTc, having a concentration of 85 μCi ml^{-1} each, and of 1.8, 3.2 and 1.3 cm diameters (inserts number

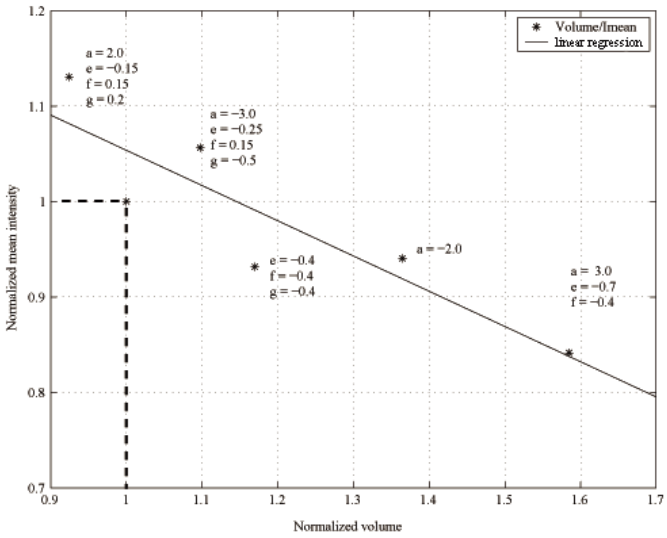

(c)

Figure 8. (Continued.)

1, 2 and 3 respectively) was acquired with a Millenium-VG SPECT camera. This camera consists of two detectors revolving around the field-of-view (FOV). Each of the detectors is of dimensions $540 \times 400 \times 15.8$ mm^3. The scanner is capable of producing data in limited angle 3D mode (i.e., with axial lead septas mounted) and in full 3D mode (i.e., without the led septas). The experiments presented here were acquired in limited 3D mode (commonly used for lungs and abdomen studies).

Five data acquisitions were performed, and for each acquisition, the phantom was translated 1 cm in the axial direction of the scanner system. By summing the sinograms, we simulate the acquisition of a moving phantom. Finally, one single acquisition of duration five times longer than every single acquisition was performed in the reference position, to serve as ground truth.

The reconstructed volumes had dimensions $128 \times 128 \times 128$ voxels with a voxel size of $4.42 \times 4.42 \times 4.42$ mm^3. As for the simulated data, the same criteria were used to select the regularization parameters. Gaussian regularization every two iterations with a full-width at half-maximum (FWHM) of 8.0 mm were set as main parameters. No other correction factors were incorporated to the reconstruction. Figure 9 shows the corrected and non-corrected reconstructed volumes.

Image segmentation performed by thresholding at a fix percentage of maximum intensity was carried out. Then, for each insert, volume, CR, and CV measurements were calculated to assess the quality of the motion compensation in phantom data. Since for the experiments the background was air, in theory CR should be infinity. Thus, to make the results understandable we compare the average activity of the lesion in a normalized intensity scale with respect to an unitary average activity of the background. In addition, volume-error-non-corrected (VENC) and volume-error-corrected (VEC) were defined as the relative error between the reference and non-corrected volumes and between the reference and corrected volumes, respectively. Centroid-error-non-corrected (CENC) and centroid-error-corrected (CEC) are defined as the distance between reference and non-corrected centroids and between reference and corrected centroids, respectively. CR ratios are presented as CR_c (corrected contrast recovery) over

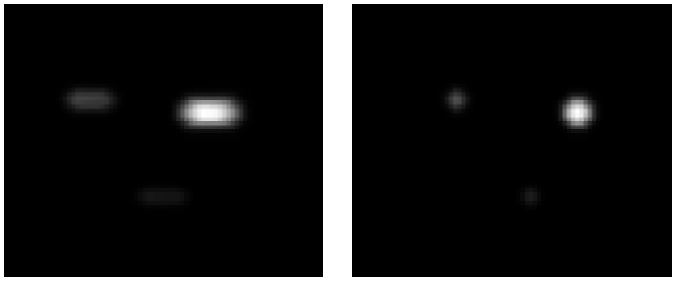

(a) Non-corrected (b) Corrected

Figure 9. Effect of discrete axial translations of sphere sources during an ET study. Without motion compensation (a) and after motion compensation (b).

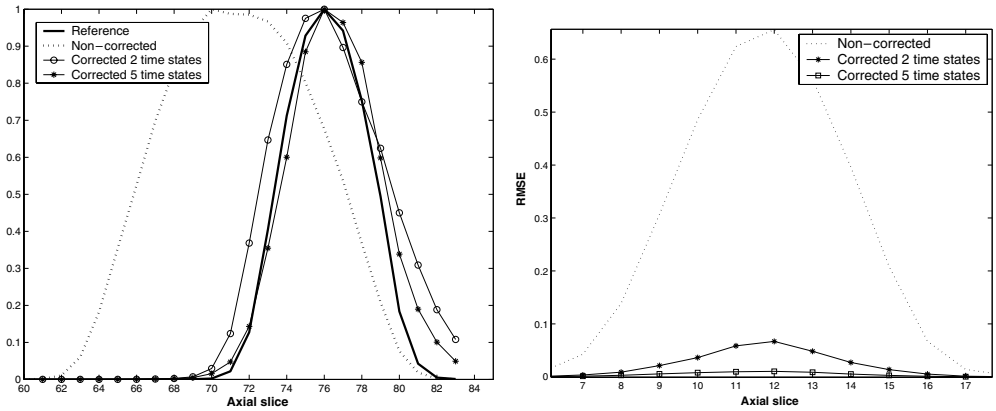

Figure 10. Phantom data. Intensity profiles of reference, non-corrected and corrected volumes of insert number two for different numbers of time states (a), and root-mean-square errors for each slice in the hot spot volume for the non-corrected and corrected reconstructed images (b).

Table 2. Results of motion correction for phantom data. Labels stand for volume-error-non-corrected (VENC), volume-error-corrected (VEC), centroid-error-non-corrected (CENC), centroid-error-corrected (CEC), corrected contrast recovery (CR_c), non-corrected contrast recovery (CR_{nc}), corrected coefficient of variability (CV_c), and non-corrected coefficient of variability (CV_{nc}).

Insert	VENC	VEC	CENC (cm)	CEC (cm)	CR_c/CR_{nc}	CV_c/CV_{nc}
1	350%	5.8%	2.0	0.16	2.2	0.58
2	125%	1%	1.96	0.21	1.62	0.89
3	166%	8%	1.85	0.21	2.57	0.48

CR_{nc} (non-corrected contrast recovery). Similarly, CV ratios are presented as CV_c (corrected coefficient of variability) over CV_{nc} (non-corrected coefficient of variability) (see table 2).

We present intensity profiles and RMSE values computed for each axial slice within the hot spot volume and for different numbers of time states, where for a given number i of time states each step of the motion discretization spans L/i cm, with L the maximum translation of the phantom with respect to the reference position (see figure 10).

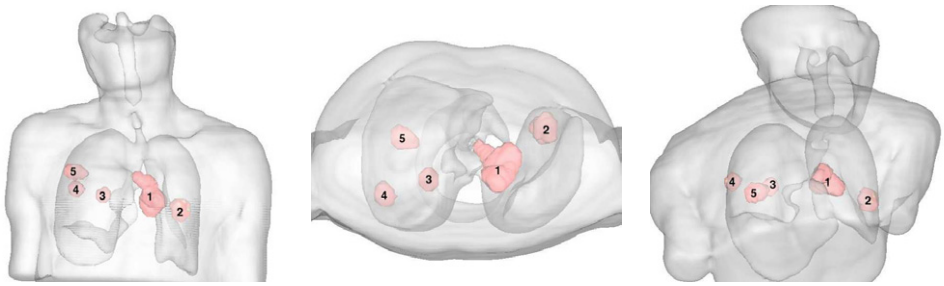

Figure 11. Different views of approximative lesion positions for the five patients. Iso-surfaces for each lesion are positioned under an average anatomy for visualization purposes. Numeric labels correspond to the patient numbers in table 3.

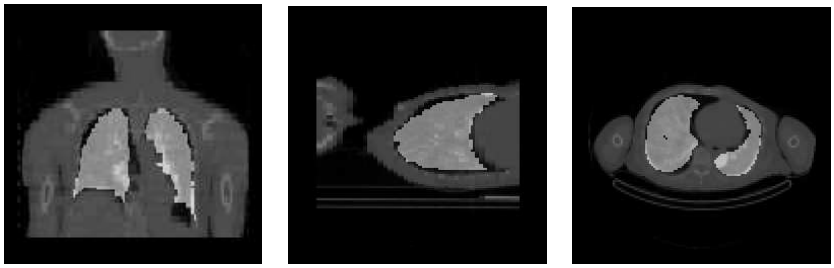

(a) Coronal (b) Sagittal (c) Axial

Figure 12. Image fusion between the patient's attenuation map and the averaged lungs anatomy of the respiratory motion model after affine registration.

Table 3. Patient database summary for respiratory motion correction tests.

Patient	Position	CT size (mm)	Surgical size (mm)
1	Left superior	60	80
2	Left medium	–	40
3	Right medium	16	–
4	Right inferior	28	–
5	Right superior	–	37

RMSE measures and visual inspection were used as criteria to evaluate the motion compensation technique. From table 2 and figure 10 it can be seen that the motion correction method yields corrected volume size and position of the spheres. From table 2 an improvement can also be noticed in both figures of merit which indicates an improvement in the spatial distribution of intensities.

3.1.4. Patient data. Five patients having one lesion each, underwent dual-head coincidence gamma camera scanning (CDET). The projection data was used to test the methodology of motion compensation presented in section 2.4. Figure 11 shows approximative positions of each lesion labeled according to table 3 which summarizes, if available, the lesion position, CT and post-surgery lesion sizes. Figure 12 shows the result after adaptation of the respiratory model to the patient's anatomy (see figure 3).

Table 4. Results of motion compensation for patients in table 3. Labels stand for contrast recovery (CR), coefficient of variability (CV) for the non-corrected (NC) and corrected (C) case, and lesion displacements in the cranial–caudal (CC), anterior–posterior (AP) and lateral (LR) directions.

Patient	Volume (C/NC)	Displacement (mm)			CR		CV	
		LR	AP	CC	NC	C	NC	C
1	0.95	2.00	3.20	3.20	4.78	5.42	0.22	0.23
2	0.64	2.60	3.60	5.10	5.04	6.06	0.24	0.20
3	0.98	0.30	2.62	4.23	7.47	7.49	0.26	0.22
4	0.86	0.45	1.20	1.74	3.66	3.90	0.18	0.16
5	0.77	2.50	0.60	2.33	4.92	5.70	0.09	0.09

For each patient in table 3, image reconstruction with and without motion compensation was performed. Discretization in three motion states and Gaussian regularization with filter full-width at half-maximum (FWHM) of 8.5 mm every three iterations were set as main parameters. The reconstructed image dimensions are $128 \times 128 \times 128$ with a voxel size of $4 \times 4 \times 4$ mm^3. As for the phantom experiments, image segmentation performed by thresholding at a fixed percentage of maximum intensity was carried out. Then, for each insert, volume, CR and CV measurements were calculated. Table 4 presents the results obtained in terms of lesion volume (normalized with respect to the non-corrected case), contrast recovery (CR), coefficient of variability (CV) for the non-corrected (NC) and corrected (C) cases, and lesion displacements in the cranial–caudal (CC), anterior–posterior (AP) and lateral (LR) directions. Figure 13 shows for patient number two, coronal, sagittal and axial slices without motion compensation (left column) and with motion compensation (central column). The right column in figure 13 is a zoom of both, the region of interest of the non-corrected (i.e. without motion compensation) image and the motion-corrected contour (extracted from the segmented image). Figure 14 shows line profiles across the lesion in patient number two. For each plane (i.e., coronal, sagittal and axial) motion-compensated and non-corrected line profiles are plotted together.

From the results presented in table 4, a reduction in the lesion volumes after motion correction, ranging from 2% to 36% can be noticed. In terms of displacements of the lesion's centroids, the cranial–caudal direction presents the maximal displacements, while the lateral direction presents the smaller ones, a fact that agrees with the findings in lung lesions displacements of Seppenwoolde and colleagues (Seppenwoolde *et al* 2002). The lesion in patient number four experiences the smallest global displacement, which is attributed to its position near the back of the thorax, where displacements are found to be minimal. On the other hand, the lesion in patient number two experiences the largest motion in the cranial–caudal direction and the largest change in volume. This is expected to happen due to the position of the lesion, where rigid structures are not expected to be attached to it (see figure 11). Quantitative measures indicate improvements in contrast recovery after motion compensation, which demonstrates the ability of the proposed method to compensate the blurring effects in the lesion area and its spatial activity distribution. Improvements in noise level are less significative. However, we did not find any increase in noise level due to motion compensation.

4. Discussion

The modeling of emission elements as spheres that deform into ellipsoids under the action of respiration is a novelty of the method. As was discussed, this modeling allows us to take

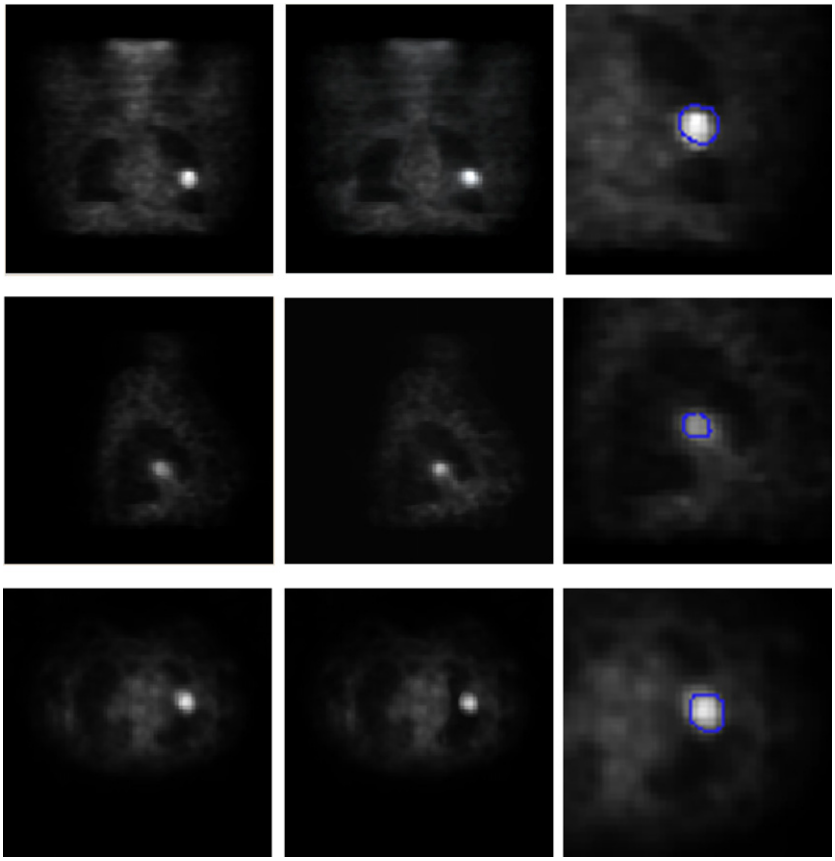

Figure 13. Coronal, sagittal and axial slices for patient number two without motion compensation (left column), with motion compensation (central column) and a zoom of both, the region of interest of the non-corrected image and the line contour of the motion-compensated lesion (right column).

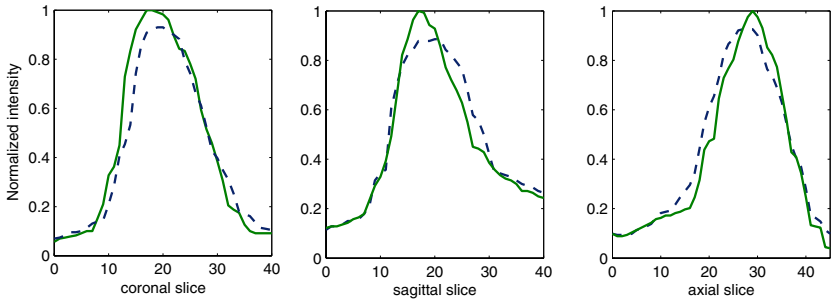

Figure 14. Line profiles across the lesion in patient number two for the coronal, sagittal and axial planes. For the coronal and sagittal plane, the line profile is taken along the cranial–caudal direction, and for the axial plane in the anterior–posterior direction (i.e., vertical line across the lesion in each plane in figure 13). For each plot, the continuous and non-continuous lines correspond to the motion-compensated and non-corrected image, respectively.

into account local deformations found inside the thorax due to respiratory motion. Is it worth noticing though, that the approaches in (Jacobson and Fessler 2003, Qiao *et al* 2006, Li *et al* 2006) also have capabilities to deal with local deformations through a motion model that is not used to rule the dynamic of the system matrix terms as proposed here but as the motion model conceived from first principles to work on emission maps at different times. A comparative study would be then of great interest.

Another issue of interest about the voxel modeling comes from the fact that although such voxel modeling can incur aliasing effects (e.g., due to the possibility that a tilted line that intersects a cubic voxel near a corner may not intersect the inscribed sphere), we noted that the effects are negligible and mostly eliminated by the regularization step. Besides, previous works on image representation and image reconstruction in 3D have shown the good properties of using spherical volume elements (or blobs) in terms of noise and contrast recovery (Lewitt 1990, Matej and Lewitt 1996). These studies have demonstrated that a configuration of blobs with a width inferior to the intrinsic resolution width of the data acquisition system provides satisfactory results in terms of image quality and noise suppression. Further research must be, however, conducted to determine precisely how these findings should be related to the proposed motion compensation methodology. Nonetheless, preliminary results and experimentation give us an indication that such a consideration holds for the proposed respiratory motion compensation scheme. Finally, another interesting point of research is how parameterized-overlapping blobs can improve the image quality of motion-compensated images, as has been shown to be the case for static tomographic reconstructed images (Matej and Lewitt 1996).

Under the initial design considerations of the method (i.e., no external respiratory tracking devices, and no data acquisition modes allowing temporal information retrieval) we have addressed the problem when no information about the patient's breathing is available. It is our belief that this corresponds to the most unfavorable case, and although it would be ideal to have the true patient's respiratory motion, this is rarely possible in clinical practice since it requires special imaging devices (e.g., 4D scanner). Some other devices could also give some information about the patient's respiratory motion (e.g., real-time position management (RPM) systems), but they are also rare in clinical routine, and have to be coupled to an imaging system.

As presented in section 2.4, the motion model is built from MRI data of a single subject. This makes the estimation of the patient-specific respiratory motion sensitive to the selection of the subject being used as a respiratory motion template. The next section discusses improvements and future work being performed to avoid this possible issue.

5. Conclusions and perspectives

During an emission tomography study, induced motion due to patient breathing can lead to artifacts in the reconstructed images. This can produce a less accurate diagnosis and, more important, an incorrect radiotherapy plan (Osman *et al* 2003, Nehmeh *et al* 2002, Seppenwoolde *et al* 2002). We have presented a methodology to compensate for respiratory motion effects that does not require any additional equipment or special data acquisition protocols. The method is based on a respiratory motion model that takes place in the computation of each term of the probability matrix and takes into account displacements and deformations experienced by the voxel during respiratory motion. For this, we model the emission elements as spheres that translate and deform into ellipsoids, which makes the implementation straightforward and allows faster computations than using classical methods of voxel/tube intersection.

The methodology was implemented in a parallel framework and tested with simulated, phantom, and patient data. The results show the ability of the proposed method to compensate for motion, rendering images with improved spatial intensity distributions and corrected lesions' shapes. Furthermore, the results obtained in simulated data to test the ellipsoidal voxel representation show improvements in volume correction when using such a voxel modeling.

We presented a respiratory motion model built from MRI data of a single subject. The model consists of a displacement vector field describing the displacements of each voxel in a discretized space, which is then adapted to the patient's anatomy through affine transformations. This voxel-wise modeling allows us to take into account the spatial deformation variability found within the breathing lungs. Furthermore, the study of local voxel deformations can be retrieved directly from the analysis of this displacement vector field, as explained in section 2.3.

We are convinced that this first approach yields images with lesser respiratory motion effects than those reconstructed without motion compensation. Indeed, improvements of the figures of merit were found after motion compensation, and volume reduction and lesion displacements are likely to occur according to findings of previous studies (Seppenwoolde *et al* 2002). Moreover, under the strong initial considerations, we believe that such an approach can make a valuable contribution in terms of retrospective motion compensation in emission tomography. This presents itself as an advantage over existing methods requiring on-site setting of the data acquisition system or the presence of external devices.

Further improvements and work in progress consider the inclusion of breathing and anatomy subject variability into the respiratory motion model estimation. In this sense, a statistical respiratory model is built not from one single subject but from a given population. This is in order to avoid possible biases introduced when using a single subject to build the motion model.

The main interest of the proposed method is on motion correction for intrapulmonary nodules. However, it is known that respiratory motion affects imaging of other organs (Langen and Jones 2001, Livieratos *et al* 1999, 2003, Klein *et al* 1998). A model considering thorax and abdomen deformations would allow us to consider deformations produced not only inside the lungs as it has been proposed here in the framework of respiratory motion compensation for lung cancer. Cardiac motion was not considered since it has been shown that its impact is of lesser extent compared to respiratory motion (Berbeco *et al* 2005).

Acknowledgments

The authors would like to thank the staff at the CAL center for their collaboration in the acquisition of phantom and patient data.

Appendix A

Given the equation of an ellipsoid in its standard form: $x^2/a^2 + y^2/b^2 + z^2/c^2 = r^2$ (for an ellipsoid $r = 1$ and for a sphere $a = b = c = 1$), and the parametric equation of a 3D line $(x_0, y_0, z_0) + t(d_x, d_y, d_z)$, in which (x_0, y_0, z_0) is a known point in the line and $d_x = x_0 - x_1, d_y = y_0 - y_1, d_z = z_0 - z_1$, with (x_1, y_1, z_1) another point in the line. The values of t defining the intersection points are found by: $t_i = -B/2A \pm \sqrt{B^2/4A^2 - C/A}$, with $A = (d_x bc)^2 + (d_y ac)^2 + (d_z ab)^2$, $B = 2(d_x x_0 b^2 c^2 + d_y y_0 a^2 c^2 + d_z z_0 a^2 b^2)$ and $C = \left(\left(bcx_0^2\right) + (acy_0)^2 + (abz_0)^2 - (rabc)^2\right)$.

Appendix B

Let us define $\varphi_i(b) : \mathbb{N} \times \mathbb{R}^3 \mapsto \mathbb{R}^3$ as the spatio-temporal transformation that describes the position of voxel index b with coordinates (x_i, y_i, z_i) at time i. For the sake of simplicity the following notation is adopted,

$$\varphi_i(b) = \varphi(i, b) = (\varphi_x(i, b), \varphi_y(i, b), \varphi_z(i, b)), \tag{B.1}$$

with $\varphi_j : \mathbb{N} \times \mathbb{R}^3 \mapsto \mathbb{R}$; $j \in \{1, 2, 3\}$.

Thus, the matrix $\nabla\varphi_i$ can be obtained as

$$\nabla\varphi_i = \left(\begin{array}{ccc} \dfrac{\partial\varphi_x}{\partial x} & \dfrac{\partial\varphi_x}{\partial y} & \dfrac{\partial\varphi_x}{\partial z} \\ \dfrac{\partial\varphi_y}{\partial x} & \dfrac{\partial\varphi_y}{\partial y} & \dfrac{\partial\varphi_y}{\partial z} \\ \dfrac{\partial\varphi_z}{\partial x} & \dfrac{\partial\varphi_z}{\partial y} & \dfrac{\partial\varphi_z}{\partial z} \end{array} \right) \Bigg|_{\substack{x = x_i \\ y = y_i \\ z = z_i}} . \tag{B.2}$$

References

Ahmed M, Yamany S, Mohamed N, Farag A and Moriarty T 2002 A modified fuzzy c-means algorithm for bias field estimation and segmentation of MRI data *IEEE Trans. Med. Imaging* **21** 193–9

Balter J, Haken R T, Lawrence T, Lam K and Robertson J 1996 Uncertainties in CT-based radiation therapy treatment planning associated with patient breathing *Int. J. Radiat. Oncol. Biol. Phys.* **36** 167–74

Berbeco R, Mostafavi H, Sharp G and Jiang S 2005 Towards fluoroscopic respiratory gating for lung tumours without radiopaque markers *Phys. Med. Biol.* **50** 4481–90

Cachier P, Bardinet E, Dormont D, Pennec X and Ayache N 2003 Iconic feature based nonrigid registration: the PASHA algorithm *Comput. Vis. Image Underst.* **89** 272–98

Camara O, Delso G and Bloch I 2002 Evaluation of a thoracic elastic registration method using anatomical constraints in oncology *2nd. Joint Conf. of the IEEE Engineering in Medicine and Biology Society*

Cao Z, Gilland D R, Mair B A and Jaszczak R J 2003 Three-dimensional motion estimation with image reconstruction for gated cardiac ECT *IEEE Trans. Nucl. Sci.* **50** 384–8

Crawford C, King K, Ritchie C and Godwin J 1996 Respiratory compensation in projection imaging using a magnification and displacement model *IEEE Trans. Med. Imaging* **15** 327–32

Gilland D R, Mair B A, Bowsher J E and Jaszczak R J 2002 Simultaneous reconstruction and motion estimation for gated cardiac ECT *IEEE Trans. Nucl. Sci.* **49** 2344–9

Gravier E and Yang Y 2005 Motion-compensated reconstruction of tomographic image sequences *IEEE Trans. Nucl. Sci.* **52** 51–6

Gravier E, Yang Y, King M A and Jin M 2006 Fully 4d motion-compensated reconstruction of cardiac spect images *Phys. Med. Biol.* **51** 4603–19

Harrison R, Vannoy S, Haynor D, Gillispie S, Kaplan M and Lewellen T 1993 Preliminary experience with the photon history generator module of a public-domain simulation system for emission tomography *Conf. Rec. IEEE Nucl. Sci. Symp.* pp 1154–8

Herman G and Odhner D 1991 Performance evaluation of an iterative image reconstruction algorithm for positron emission tomography *IEEE Trans. Med. Imaging* **10** 336–46

Jacobson M W and Fessler J A 2003 Joint estimation of image and deformation parameters in motion-corrected PET *IEEE Nucl. Sci. Symp. Med. Imag. Conf.* vol 5 pp 3290–4

Klein G, Reutter B, Ho M, Reed J and Huesman R 1998 Real-time system for respiratory-cardiac gating in positron tomography *IEEE Trans. Nucl. Sci.* **45** 2139–43

Lamare F, Cresson T, Savean J, Cheze Le Rest C, Reader A J and Visvikis D 2007 Respiratory motion correction for PET oncology applications using affine transformation of list mode data *Phys. Med. Biol.* **52** 121–40

Langen K and Jones D 2001 Organ motion and its management *Int. J. Radiat. Oncol. Biol. Phys.* **50** 265–78

Levkovitz R, Falikman D, Zibulevsky M, Ben-Tal A and Nemirovski A 2001 The design and implementation of COSEM, an iterative algorithm for fully 3-D listmode data *IEEE Trans. Med. Imaging* **20** 633–42

Lewitt R M 1990 Multidimensional digital image representations using generalized Kaiser–Bessel window functions *J. Opt. Soc. Am.* A **7** 1834–46

Li T, Thorndyke B, Schreibmann E, Yang Y and Xing L 2006 Model-based image reconstruction for four-dimensional pet *Med. Phys.* **33** 1288–98

Livieratos L, Bloomfield P, Bailey D, Rhodes O, Jones T and Camici P 1999 Cardiac and respiratory gating of list-mode data on a high sensitivity PET scanner, the ECAT EXACT3D *J. Nucl. Cardiology* **6** (S16)

Livieratos L, Rajappan K, Bailey D, Rimoldi O and Camici P 2003 Respiratory gating of cardiac PET *J. Nucl. Med.* **30** (S174)

Lu W and Mackie T 2002 Tomographic motion detection and correction directly in sinogram space *Phys. Med. Biol.* **47** 1267–84

Matej S and Lewitt R M 1996 Practical considerations for 3-D image reconstruction using spherically symmetric volume elements *IEEE Trans. Med. Imaging* **15** 68–78

Mattes D, Haynor D, Vesselle H, Lewellen T and Eubank W 2003 PET-CT image registration in the chest using free-form deformations *IEEE Trans. Med. Imaging* **22** 120–8

Nehmeh S, Erdi Y, Ling C, Rosenzweig K, Schroder H, Larson S, Macapinlac H, Squire O and Humm J 2002 Effect of respiratory gating on quantifying PET images of lung cancer *J. Nucl. Med.* **43** 876–81

Nehmeh S, Erdi Y, Rosenzweig K, Schroder H, Larson S, Squire O and Humm J 2003 Reduction of respiratory motion artifacts in PET imaging of lung cancer by respiratory correlated dynamic PET: Methodology and comparison with respiratory gated PET *J. Nucl. Med.* **44** 1644–8

Osman M, Cohade C, Nakamoto Y, Marshall L, Leal J and Wahl R 2003 Clinically significant inaccurate localization of lesions with PET/CT: frequency in 300 patients *J. Nucl. Med.* **4** 240–3

Osman M, Cohade C, Nakamoto Y and Wahl R 2003 Respiratory motion artifacts on PET emission images obtained using CT attenuation correction on PET-cT *J. Nucl. Med.* **30** 603–6

Ourselin S, Roche A, Prima S and Ayache N 2000 Block matching: a general framework to improve robustness of rigid registration of medical images *3rd Int. Conf. on Medical Robotics, Imaging and Computer Assisted Surgery (MICCAI 2000)* (*Lectures Notes in Computer Science* vol 1935) ed A DiGioia and S Delp (Pittsburgh, PA: Springer) pp 557–66

Pellot-Barakat C, Ivanovic M, Herment A, Erlandsson K and Shelton D 2001 Detection of motion in hybrid PET/SPECT imaging based on the correlation of partial sinograms *IEEE Trans. Med. Imaging* **20** 1072–83

Picard Y and Thompson C 1997 Motion correction of PET images using multiple acquisition frames *IEEE Trans. Med. Imaging* **16** 137–44

Qi J and Huesman R H 2002 List mode reconstruction for PET with motion compensation: a simulation study *IEEE Int. Symp. Biol. Imaging* pp 413–6

Qiao F, Pan T, Clark J W and Mawlawi O R 2006 A motion-incorporated reconstruction method for gated PET studies *Phys. Med. Biol.* **51** 3769–83

Rahmim A and Bloomfield P 2003 Motion correction in histogram-mode and listmode EM reconstructions *IEEE MIC*

Rahmim A, Bloomfield P, Houle S, Lenox M, Michel C, Buckley K R, Ruth T J and Sossi V 2004 Motion compensation in histogram-mode and list-mode EM reconstructions: Beyond the event-driven approach *IEEE Trans. Nucl. Sci.* **51** 2588–96

Reader A, Ally S, Bakatselos F, Manavaki R, Walledge R, Jeavons A, Julyan P, Zhao S, Hastings D and Zweit J 2002 One-pass list-mode EM algorithm for high resolution 3D PET image reconstruction into large arrays *IEEE Trans. Nucl. Sci.* **49** 693–9

Rey D, Subsol G, Delingette H and Ayache N 2002 Automatic detection and segmentation of evolving processes in 3D medical images: application to multiple sclerosis *Med. Image Anal.* **6** 163–79

Segars W 2001 Development of a new dynamic NURBS-based cardiac-torso (NCAT) phantom *PhD Thesis*The University of North Carolina

Seppenwoolde Y, Shirato H, Kitamura K, Shimizu S, van Herk M, Lebesque J and Miyasaka K 2002 Precise and real-time measurement of 3D tumor motion in lung due to breathing and heartbeat, measured during radiotherapy *Int. J. Radiat. Oncol. Biol. Phys.* **53** 822–34

Shepp L and Vardi Y 1982 Maximum likelihood reconstruction for emission tomography *IEEE Trans. Med. Imaging* **1** 113–22

Shih H, Jiang S, Aljarrah K, Dopke K and Choi N 2002 Planning target volume determined with fused CT images of fast, breath-hold, and four second simulation CT scans to account for respiratory movement in 3D-CRT in lung cancer *Annual Meeting of The American Society for Therapeutic Radiology and Oncology* (New Orleans, LA)

Shimizu S, Shirato H, Kagei K, Nishioka T, Bo X, Dosaka-Akita H, Hashimoto S, Aoyama H, Tsuchiya K and Miyasaka K 2000 Impact of respiratory movement on the computed tomographic images of small lung tumors in three-dimensional (3D) radiotherapy *Int. J. Radiat. Oncol. Biol. Phys.* **46** 1127–33

Siddon R 1985 Fast calculation of the exact radiological path for a three-dimensional CT array *Med. Phys.* **12** 252–5

Thielemans K, Mustafovic S and Schnorr L 2003 Image reconstruction of motion corrected sinograms *IEEE Med. Imaging Conf.*

Vedam S, Kini V, Keall P, Ramakrishnan V, Mostafavi H and Mohan R 2003 Quantifying the predictability of diaphragm motion during respiration with a noninvasive external marker *Med. Phys.* **30** 505–13

Visvikis D, Barret O, Fryer T, Turzo A, Lamare F, Cheze Le Rest C and Bizais Y 2003 *A posteriori* respiratory motion gating of dynamic pet images *IEEE Nucl. Sci. Symp. Conf. Rec.* vol 5 pp 3276–80

Weruaga L, Morales J, Núñez L and Verdú R 2003 Estimating volumetric motion in human thorax with parametric matching constraints *IEEE Trans. Med. Imaging* **22** 766–72